



LAWRENCE  
LIVERMORE  
NATIONAL  
LABORATORY

# Improved Multiple-Coarsening Methods for Sn Discretizations of the Boltzmann Equation

B. Lee

December 1, 2008

## **Disclaimer**

---

This document was prepared as an account of work sponsored by an agency of the United States government. Neither the United States government nor Lawrence Livermore National Security, LLC, nor any of their employees makes any warranty, expressed or implied, or assumes any legal liability or responsibility for the accuracy, completeness, or usefulness of any information, apparatus, product, or process disclosed, or represents that its use would not infringe privately owned rights. Reference herein to any specific commercial product, process, or service by trade name, trademark, manufacturer, or otherwise does not necessarily constitute or imply its endorsement, recommendation, or favoring by the United States government or Lawrence Livermore National Security, LLC. The views and opinions of authors expressed herein do not necessarily state or reflect those of the United States government or Lawrence Livermore National Security, LLC, and shall not be used for advertising or product endorsement purposes.

This work performed under the auspices of the U.S. Department of Energy by Lawrence Livermore National Laboratory under Contract DE-AC52-07NA27344.

# IMPROVED MULTIPLE-COARSENING METHODS FOR SN DISCRETIZATIONS OF THE BOLTZMANN EQUATION

B. LEE \*

**Abstract.** In a recent series of articles, the author presented a multiple-coarsening multigrid method for solving  $S_n$  discretizations of the Boltzmann transport equation. This algorithm is applied to an integral equation for the scalar flux or moments. Although this algorithm is very efficient over parameter regimes that describe realistic neutron/photon transport applications, improved methods that can reduce the computational cost are presented in this paper. These improved methods are derived through a careful examination of the frequencies, particularly the near-nullspace, of the integral equation. In the earlier articles, the near-nullspace components were shown to be smooth in angle in the sense that the angular fluxes generated by these components are smooth in angle. In this paper, we present a spatial description of these near-nullspace components. Using the angular description of the earlier papers together with the spatial description reveals the intrinsic space-angle dependence of the integral equation's frequencies. This space-angle dependence is used to determine the appropriate space-angle grids to represent and efficiently attenuate the near-nullspace error components on. It will be shown that these components can have multiple spatial scales. By using only the appropriate space-angle grids that can represent these spatial scales in the original multiple-coarsening algorithm, an improved algorithm is obtained. Moreover, particularly for anisotropic scattering, recognizing the strong angle dependence of the angular fluxes generated by the high frequencies of the integral equation, another improved multiple-coarsening scheme is derived. Restricting this scheme to the appropriate space-angle grids produces a very efficient method.

**Key words.** Boltzmann equation, transport, multigrid method, Sn discretizations, anisotropic scattering.

**AMS(MOS) subject classifications.** 65M55, 65M70, 65N55, 65R20, 65Z05

**1. Introduction.** Let  $R$  and  $S^2$  respectively be a bounded region of  $\mathbb{R}^2$  or  $\mathbb{R}^3$ , and the unit sphere. For simplicity, we assume that  $R$  is of unit diameter. The Cartesian product  $R \times S^2$  is a space-angle domain. We are interested in the steady-state mono-energetic Boltzmann transport equation defined in this domain:

$$(1.1) \quad [\Omega \cdot \nabla + \sigma_t(\mathbf{x})] \psi(\mathbf{x}, \Omega) = \int d\Omega' \sigma_s(\mathbf{x}, \Omega \cdot \Omega') \psi(\mathbf{x}, \Omega') + q(\mathbf{x}, \Omega) \quad (\mathbf{x}, \Omega) \in R \times S^2$$

$$(1.2) \quad \psi(\mathbf{x}, \Omega) = g(\mathbf{x}, \Omega) \quad \mathbf{n} \cdot \Omega < 0, \mathbf{x} \in \partial R.$$

This boundary value problem describes the equilibrium state of neutrons/photons propagating through a medium. It describes the transport of a stream of neutrons/photons in the presence of a source, and as these particles collide with the nuclei of matter. Such collisions can result in scattering, when the incoming particle continues its flight after the collision but with altered direction, or in absorption, when the incoming particle is absorbed and no particle of the same type is emitted. The probabilities for these interactions are determined by the medium's cross-sections. In this equation,  $\psi$  is the angular flux of the particles,  $\sigma_t$  and  $\sigma_s$  are respectively the medium's total and scattering cross-sections (the absorption cross-section is  $\sigma_a := \sigma_t - \sigma_s$ ), and  $q$  is the external source. The directional derivative ( $\Omega \cdot \nabla$ ) describes the streaming process of particles, and the integral quantity describes the scattering process of particles incoming at angle  $\Omega'$  and scattered to angle  $\Omega$ . The physical quantity of interest is the angle-integrated quantity

$$(1.3) \quad \phi(\mathbf{x}) = \int d\Omega \psi(\mathbf{x}, \Omega),$$

the scalar flux. One might also be interested in the scalar moments

$$(1.4) \quad \phi_{jm}(\mathbf{x}) = \int d\Omega Y_{jm}(\Omega) \psi(\mathbf{x}, \Omega),$$

---

\*Center for Applied Scientific Computing, Lawrence Livermore National Laboratory, Livermore, CA. *email:* lee123@llnl.gov. This work performed under the auspices of the U.S. Department of Energy by Lawrence Livermore National Laboratory under Contract DE-AC52-07NA27344.

where  $Y_{jm}$ ,  $j = 0, \dots, L$ ,  $m = -j, \dots, j$ , is the  $jm$ 'th spherical harmonic ([20]). In particular, the scalar moments often are needed when the scattering kernel is angle dependent and expressed as a truncated,  $(L + 1)^2$ -term, spherical harmonic expansion, i.e., when the scatterer is anisotropic. When the scattering kernel is angle independent, i.e., the scatterer is isotropic, only the scalar flux is needed.

A discretization of this high-dimensional problem involves an angular and spatial component. The most common approach is to collocate in angle and finite-difference, finite-volume, or finite-element in space. As in [8], we refer to this approach as a  $S_n$  discretization.

The linear system generated by a  $S_n$  discretization is exceptionally large. For example, assume that  $nd$  angle collocation points are used. They are chosen to be the points of a quadrature rule satisfying

$$\int d\Omega \sigma_s(\mathbf{x}, \Omega \cdot \Omega') \psi(\mathbf{x}, \Omega) \approx \sum_{i=1}^{nd} w_i \sigma_s(\mathbf{x}, \Omega_i \cdot \Omega') \psi(\mathbf{x}, \Omega_i),$$

where the  $w_i$ 's are the quadrature weights. For each collocation angle  $\Omega_i$ , the streaming-■ collision operator

$$[\Omega \cdot \nabla + \sigma_t]$$

is replaced with

$$(1.5) \quad [\Omega_i \cdot \nabla + \sigma_t].$$

Let the spatial discretizing of (1.5) be denoted by  $\mathbf{H}_i^h$ . Then the generated linear system has the form

$$(1.6) \quad \left[ \begin{array}{c|c} \mathbf{H}^h & \mathbf{B}^h \\ \mathbf{C}^h & \mathcal{I}^h \end{array} \right] \begin{pmatrix} \mathbf{u}^h \\ \mathbf{w}^h \end{pmatrix} = \begin{pmatrix} \mathbf{b}^h \\ \mathbf{0} \end{pmatrix},$$

with

$$\begin{aligned} \mathbf{H}^h &= \begin{bmatrix} \mathbf{H}_1^h & & & \\ & \mathbf{H}_2^h & & \\ & & \ddots & \\ & & & \mathbf{H}_{nd}^h \end{bmatrix} & \mathcal{I}^h &= \begin{bmatrix} \mathbf{I}_{0,0}^h & & & \\ & \mathbf{I}_{1,-1}^h & & \\ & & \ddots & \\ & & & \mathbf{I}_{L,L}^h \end{bmatrix} \\ \mathbf{B}^h &= \begin{bmatrix} -(Y_{0,0})_1 \mathbf{T}^h \sigma_{s,0}^h & -(Y_{1,-1})_1 \mathbf{T}^h \sigma_{s,1}^h & \cdots & -(Y_{L,L})_1 \mathbf{T}^h \sigma_{s,L}^h \\ \vdots & \vdots & \vdots & \vdots \\ -(Y_{0,0})_{nd} \mathbf{T}^h \sigma_{s,0}^h & -(Y_{1,-1})_{nd} \mathbf{T}^h \sigma_{s,1}^h & \cdots & -(Y_{L,L})_{nd} \mathbf{T}^h \sigma_{s,L}^h \end{bmatrix} \\ \mathbf{C}^h &= \begin{bmatrix} -w_1 (Y_{0,0})_1 \mathbf{S}^h & -w_2 (Y_{0,0})_2 \mathbf{S}^h & \cdots & -w_{nd} (Y_{0,0})_{nd} \mathbf{S}^h \\ \vdots & \vdots & \vdots & \vdots \\ -w_1 (Y_{L,L})_1 \mathbf{S}^h & -w_2 (Y_{L,L})_2 \mathbf{S}^h & \cdots & -w_{nd} (Y_{L,L})_{nd} \mathbf{S}^h \end{bmatrix} \\ \mathbf{u}^h &= \begin{pmatrix} \psi_1^h \\ \psi_2^h \\ \vdots \\ \psi_{nd}^h \end{pmatrix} & \mathbf{w}^h &= \begin{pmatrix} \phi_{0,0}^h \\ \phi_{1,-1}^h \\ \vdots \\ \phi_{L,L}^h \end{pmatrix} & \mathbf{b}^h &= \begin{pmatrix} \mathbf{q}_1^h \\ \mathbf{q}_2^h \\ \vdots \\ \mathbf{q}_{nd}^h \end{pmatrix}, \end{aligned}$$

and where the  $\mathbf{I}_{l,m}^h$ 's are identity matrices, the  $\sigma_{s,l}^h$ 's are the spherical harmonic expansion coefficients of the scattering kernel, the  $(Y_{jm})_i$ 's are the spherical harmonics evaluated at the angle quadrature point  $\Omega_i$ , and the  $\mathbf{T}^h$  and  $\mathbf{S}^h$  are operators mapping the scalar moment vectors to angular flux vectors and vice versa, as these vectors

can be defined on staggered grids (see [9] for more details). Applying block Gauss elimination to (1.6), the discrete integral equation for the scalar moments is

$$(1.7) \quad [\mathcal{I}^h - \mathbf{C}^h [\mathbf{H}^h]^{-1} \mathbf{B}^h] \mathbf{w}^h = -\mathbf{C}^h [\mathbf{H}^h]^{-1} \mathbf{b}^h.$$

Since discrete integral operator  $\mathbf{C}^h [\mathbf{H}^h]^{-1} \mathbf{B}^h$  is spatially and angularly dependent, (1.7) is a high-dimensional equation.

The multigrid method proposed in [8] and [9] is applied directly to integral equation (1.7). Because of the high-dimensionality of the equation, this is a high-dimensional multigrid method. Its structure is tree shaped: the angle grid is coarsened along the trunk while the spatial grid is coarsened along the branches sprouting off the trunk (see Figure 1.1, left diagram). A V-cycle for this method consists of a

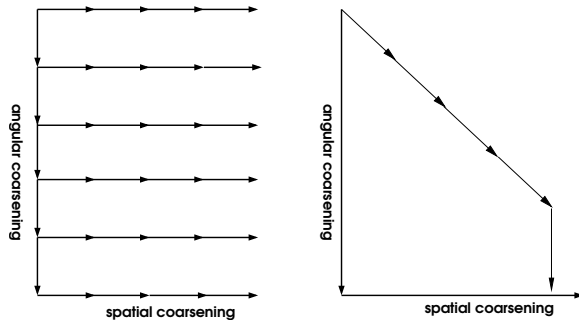


FIG. 1.1. Branched multigrid scheme. Left: coarsening in angle, with each angle-level problem coarsening in space. Right: aggressive coarsening, aggressive simultaneous coarsening in angle and space.

descent down the angle trunk, but at each angle level, a descent and ascent (i.e., a V-cycle) along the spatially coarsened branch is performed. Coarsening only in angle or in space respectively produces the vertical trunk or the top horizontal branch of Figure 1.1, left (c.f., [15] and [21], which present a method that essentially coarsens only in space), and aggressively coarsening in angle and space simultaneously produces the diagonal trunk of Figure 1.1, right. Coarsening angle and space using the full tree structure, this multigrid method can be viewed as a multiple-coarsening or semi-coarsening method: viewing each angle-level branch as a coarsening of the target integral equation, we have the multiple-coarsening viewpoint; viewing each angle-level branch as a “plane solve” ([22]) over the spatial grid, we have the semi-coarsening viewpoint.

This multiple-coarsening/semi-coarsening structure is the first component of the method in [8] and [9]. The second component is the choice of the “smoother.” As the continuous integral is compact, rather than using a smoother, a Krylov rougher is used ([12]). Compactness implies that the full operator has a cluster of eigenvalues at 1. Hence, such a rougher would capture the high-frequency components (eigenvectors with eigenvalues  $\approx 1$ ) well and some of the smooth frequency components. Capturing some of the smooth components is critical. Assuming that the discrete integral operators are collectively compact ([3]), the eigenvalue distribution and the required damping of the level rougher requisites good reduction of the smooth components on the coarser grids.

In [9], it was shown that these smooth frequencies can be represented and efficiently handled on the coarser angle levels. A quantitative description of these components was obtained by examining the continuous integral operator. For isotropic scattering, these components are approximations to  $\phi$ 's such that the solution to

$$(\Omega \cdot \nabla + \sigma_t)w = \sigma_s \phi,$$

is predominantly isotropic and approximately equal to  $\phi$  itself. That is, in terms of its spherical harmonic expansion,  $w$  is dominated by its zero'th moment and

this moment is approximately  $\phi$  itself. Such description only describes the angular dependence of these smooth frequencies. (Actually, the angular dependence of the generating angular fluxes, although these smooth frequencies are directly related to these angular fluxes.) Nevertheless, it does explain why angle coarsening is needed.

In this paper, we give a refined description of these smooth frequencies and the oscillatory frequencies. In particular, we give a spatial description and a refined angular-dependence description for all frequencies. The spatial description shows further why an effective multigrid method must coarsen in space and angle. More importantly, it describes the appropriate space-angle grids that must be used in the multigrid algorithm. Limiting the multiple-coarsening method to these space-angle grids, instead of having the tree structure of Figure 1.1, the method will have the tree structures of Figure 1.2. Clearly, this will improve the computational efficiency of the multiple-coarsening algorithm. As for the angle-dependence description, it reveals that particularly for anisotropic scattering, an alternative multiple-coarsening scheme should be used. This alternative scheme can be applied only on the appropriate space-angle grids.

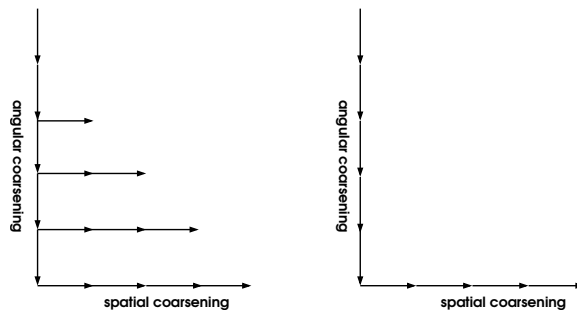


FIG. 1.2. *Improved coarsening. Left: spatial coarsening is progressively introduced. Right: spatial coarsening is introduced only on the coarsest angle branch, where the near-nullspace components can be handled efficiently.*

This paper is organized as follow. In section 2, the multiple-coarsening algorithm of [8] is given, as well as an alternative multigrid scheme that is derived by taking the semi-coarsening viewpoint of the multiple-coarsening method. Numerical results presented in this section show that this alternative method is more appropriate for anisotropic scattering. In section 3, the spatial dependence of the near-nullspace components is described. It will be shown that these smooth frequencies can have multiple spatial scales, with the scales determined by the size of the subregions where the problem is optically thick. In section 4, using the spatial-dependence description together with the angle-dependence description of these frequencies, the appropriate space-angle grids are described. Also described in this section is the strong angle dependence of the high frequencies, which will be used to explain the improved performance of the alternative scheme presented in section 2. As mentioned earlier, the implication of using only these grids in the multiple-coarsening algorithm of [8] is a multigrid scheme with the tree structure of Figure 1.2. Restricting the alternative method to these space-angle grids also produces a sparse tree structure (see Figure 2.1). Numerical results showing that these new algorithms do perform as expected are given.

**2. Multiple-Coarsening Method of [8].** The method of [8] is applied to equation (1.7). We consider only the isotropic scattering problem. Succinctly, this method coarsens in angle, and then for each angle-level branch, the algorithm coarsens in space. Figure 1.1, left diagram, illustrates the structure. As shown in [9], angle coarsening is needed to efficiently damp out error components that belong to the near-nullspace of *integral equation* (1.7).

The coarse-grid operators on the coarser levels are obtained by re-discretizing (1.7) on the coarser space-angle grids using the same  $S_n$  discretization of the target fine grid, i.e., non-standard discretization techniques are not needed on the coarser levels. This is different from the DSA methods of, for example, [1], [2], and [5], which can be viewed as two-level angle-coarsening methods, where “consistent” discretizations (i.e., non-standard coarse-grid discretizations) are needed on the coarse angle level. In terms of multilevel principles, both the method of [8] and the DSA methods try to handle slowly converging near-nullspace components on the coarser angle levels. But the fundamental difference is that the former method considers these components directly from the integral equation operator, whereas the latter methods considers these components indirectly through the integro-differential Boltzmann operator (i.e., the continuous diffusion equation used in the DSA methods is derived from the first 4 equations of the  $P_n$  formulation of the Boltzmann equation). Thus, the method of [8] simply can use the same  $S_n$  discretization on the coarser levels, while the DSA methods must use consistent discretizations, which must lead to the diffusion limit of the fine-level  $S_n$  discretization, of the DSA operator on the coarse angle level.

Turning to the details of the method of [8], let  $R$  be approximated by a discretized grid  $G^h$ , and let

$$G^{l_1} \subset G^{l_2} \subset \dots \subset G^{L_R-1} \subset G^{L_R} = G^h$$

be a nested hierarchy of spatial grids for target space grid  $G^h$ . There are  $L_R$  levels, with levels  $l_1$  and  $L_R$  being the coarsest and finest grids, respectively. To coarsen  $S^2$ , the number of angular collocation points are simply halved. Since Gauss-Legendre type quadrature rules are often used, the hierarchy of angular collocation point sets are generally non-nested. Further, to ensure that numerical integration is reasonable, the number of quadrature points on the coarsest angle level is determined by the degree of anisotropy in the scattering coefficient. When the scattering coefficient is isotropic, only 4 angles can be used on the coarsest angle level. We will assume that there are  $L_\Omega$  levels with  $L_\Omega$  denoting the finest angle grid.

On any angle level, the whole spatial hierarchy is used. Respectively denote the angle and spatial levels by  $l_\Omega$  and  $l_R$ . The level  $l_\Omega - l_R$  integral operator is then

$$[\mathbf{I}^{l_\Omega, l_R} - \mathbf{K}^{l_\Omega, l_R}] = \left[ \mathbf{I}^{l_\Omega, l_R} - \sum_{i=1}^{nd_{l_\Omega}} w_i \mathbf{S}^{l_R} [\mathbf{H}_i^{l_R}]^{-1} \mathbf{T}^{l_R} \sigma_s^{l_R} \right],$$

where  $nd_{l_\Omega}$  is the number of angular points on level  $l_\Omega$ , and  $\mathbf{S}, \mathbf{H}_i$ , and  $\sigma_s$  are indexed only by  $l_R$  because they are angle-level independent.

Both space and angle integrid transfer operators are needed. As for spatial transfer operators, let  $\hat{\mathbf{I}}_{l_R}^{l_R+1}$  and  $\mathbf{I}_{l_R+1}^{l_R}$  denote the interpolation and restriction operators between spatial levels  $l_R$  and  $(l_R + 1)$ . For example, they can be bi/trilinear interpolation and full-weighting restriction, respectively. Restriction  $\mathbf{I}_{l_R+1}^{l_R}$  is used to transfer spatial level  $(l_R + 1)$  vectors to spatial level  $l_R$  vectors, while the coarse-grid correction is interpolated using a Nystrom interpolation process ([3], [4], [13]): For fixed angle level  $l_\Omega$ , given an approximation  $\phi^{l_\Omega, l_R+1, i}$  on spatial level  $(l_R + 1)$ , the error equation for correction  $\mathbf{e}^{l_\Omega, l_R+1}$  is

$$\begin{aligned} [\mathbf{I}^{l_\Omega, l_R+1} - \mathbf{K}^{l_\Omega, l_R+1}] \mathbf{e}^{l_\Omega, l_R+1} &= \mathbf{r}^{l_\Omega, l_R+1} - [\mathbf{I}^{l_\Omega, l_R+1} - \mathbf{K}^{l_\Omega, l_R+1}] \phi^{l_\Omega, l_R+1, i} \\ &:= \mathbf{r}^{l_\Omega, l_R+1}, \end{aligned}$$

producing

$$\mathbf{e}^{l_\Omega, l_R+1} = \mathbf{K}^{l_\Omega, l_R+1} \mathbf{e}^{l_\Omega, l_R+1} + \mathbf{r}^{l_\Omega, l_R+1}.$$

Given the spatial level  $l_R$  solution  $\mathbf{e}^{l_\Omega, l_R}$ , Nystrom interpolation, denoted by  $\mathbf{I}_{l_\Omega, l_R}^{l_\Omega, l_R+1}$ , is defined by the affine process

$$(2.1) \quad \mathbf{I}_{l_\Omega, l_R}^{l_\Omega, l_R+1} \mathbf{e}^{l_\Omega, l_R} := \hat{\mathbf{I}}_{l_R}^{l_R+1} \mathbf{K}^{l_\Omega, l_R} \mathbf{e}^{l_\Omega, l_R} + \mathbf{r}^{l_\Omega, l_R+1}.$$

This is the Nystrom interpolation used in [21]. For discontinuous cross-sections with mild jumps, a better but more expensive Nystrom process is

$$(2.2) \quad \mathbf{I}_{l_\Omega, l_R}^{l_\Omega, l_R+1} \mathbf{e}^{l_\Omega, l_R} := \mathbf{K}^{l_\Omega, l_R+1} \hat{\mathbf{I}}_{l_R}^{l_R+1} \mathbf{e}^{l_\Omega, l_R} + \mathbf{r}^{l_\Omega, l_R+1}$$

since this generates an operator-dependent interpolation operator.

As for the angle integrid transfer operators, since the unknowns (and corrections) are the angle independent scalar flux or moments, the identity operator can be used for restricting between angle levels. The identity operator can also be used to transfer coarse angle vectors to fine angle vectors but a Nystrom process should be used to interpolate the angular coarse-grid correction:

$$(2.3) \quad \mathbf{I}_{l_\Omega}^{l_\Omega+1} \mathbf{e}^{l_\Omega, L_R} := \mathbf{K}^{l_\Omega+1, L_R} \mathbf{e}^{l_\Omega, L_R} + \mathbf{r}^{l_\Omega+1, L_R}.$$

Note that between any two angle levels, this Nystrom process is applied to vectors on the targeted  $L_R$  spatial grid. Note further that while the kernel in Nystrom operator (2.2) refines in space with the angular grid fixed, the kernel in (2.3) refines in angle with the spatial grid fixed.

With these integrid operators, the two angle grid algorithm can be given. As can be inferred from Figure 1.1, the angle level smoother is a spatial  $\mathbf{V}(\beta_1, \beta_2)$  cycles.

### Multiple-Coarsening/Semi-Coarsening Two-Grid $\mathbf{V}(\nu_1, \nu_2)$ Cycle

Given  $\phi_i^{L_\Omega, L_R}$  and a righthand side  $\mathbf{f}^{L_\Omega, L_R}$  on the finest level  $(L_\Omega, L_R)$ ,

1. pre-smooth: with  $\hat{\phi}_0^{L_\Omega, L_R} = \phi_i^{L_\Omega, L_R}$  apply  $\nu_1$  spatial  $\mathbf{V}(\beta_1, \beta_2)$  cycles on

$$(2.4) \quad [\mathbf{I}^{L_\Omega, L_R} - \mathbf{K}^{L_\Omega, L_R}] \hat{\phi}^{L_\Omega, L_R} = \mathbf{f}^{L_\Omega, L_R}$$

to obtain  $\hat{\phi}_{\nu_1}^{L_\Omega, L_R}$

2. residual calculation: since the restriction operator is the identity,

$$\begin{aligned} \mathbf{f}^{l_\Omega, L_R} &= \mathbf{I}_{L_\Omega}^{l_\Omega} \mathbf{r}^{L_\Omega, L_R} \\ &= \mathbf{f}^{L_\Omega, L_R} - [\mathbf{I}^{L_\Omega, L_R} - \mathbf{K}^{L_\Omega, L_R}] \hat{\phi}_{\nu_1}^{L_\Omega, L_R} \end{aligned}$$

3. coarse-grid problem: solve

$$[\mathbf{I}^{l_\Omega, L_R} - \mathbf{K}^{l_\Omega, L_R}] \mathbf{e}^{l_\Omega, L_R} = \mathbf{f}^{l_\Omega, L_R}$$

4. coarse-grid correction with angle Nystrom interpolation (2.3):

$$\hat{\phi}_{\nu_1}^{L_\Omega, L_R} \leftarrow \hat{\phi}_{\nu_1}^{L_\Omega, L_R} + \mathbf{I}_{l_\Omega}^{L_\Omega} \mathbf{e}^{l_\Omega, L_R}$$

5. post-smooth: with  $\hat{\phi}_{\nu_1}^{L_\Omega, L_R}$  apply  $\nu_2$  spatial  $\mathbf{V}(\beta_1, \beta_2)$  cycles on (2.4) to obtain  $\hat{\phi}_{\nu_1+\nu_2}^{L_\Omega, L_R}$

6. update the two-grid iterate:

$$\phi_{i+1}^{L_\Omega, L_R} = \hat{\phi}_{\nu_1+\nu_2}^{L_\Omega, L_R}.$$

Omitting the angle superscript, a spatial  $\mathbf{V}(\beta_1, \beta_2)$  cycle is given recursively by

### Spatial $\mathbf{V}(\beta_1, \beta_2)$ Cycle

Given  $\phi^{L_R}$  and  $\mathbf{f}^{L_R}$ , and setting  $level = L_R$ , call  $\mathbf{MG}(\beta_1, \beta_2, level, \phi^{level}, \mathbf{f}^{level})$ .

$\mathbf{MG}(\beta_1, \beta_2, level, \phi^{level}, \mathbf{f}^{level})$ :

1. if  $level = l_1$ , solve the coarsest level problem

$$[\mathbf{I}^{l_1} - \mathbf{K}^{l_1}] \phi^{l_1} = \mathbf{f}^{l_1}$$

2. else

(a) pre-smooth: with  $\hat{\phi}_0^{level} = \phi^{level}$  apply  $\beta_1$  spatial smoothing steps to

$$(2.5) \quad [\mathbf{I}^{level} - \mathbf{K}^{level}] \phi^{level} = \mathbf{f}^{level}$$

to obtain  $\hat{\phi}_{\beta_1}^{level}$

(b) residual calculation: compute

$$\mathbf{r}^{level} = \mathbf{f}^{level} - [\mathbf{I}^{level} - \mathbf{K}^{level}] \hat{\phi}_{\beta_1}^{level}$$

(c) restriction of residual:

$$\mathbf{f}^{(level-1)} = \mathbf{I}_{level}^{(level-1)} \mathbf{r}^{level}$$

(d) recursive call to  $\mathbf{MG}(\beta_1, \beta_2, (level - 1), \mathbf{0}, \mathbf{f}^{(level-1)})$

(e) coarse-grid correction with spatial Nystrom interpolation (2.2):

$$\hat{\phi}_{\beta_1}^{level} \leftarrow \hat{\phi}_{\beta_1}^{level} + \mathbf{I}_{(level-1)}^{level} \phi^{(level-1)}$$

(f) post-smooth: with  $\hat{\phi}_{\beta_1}^{level}$  apply  $\beta_2$  spatial smoothing steps to (2.5) to

obtain  $\hat{\phi}_{\beta_1+\beta_2}^{level}$

(g) update iterate:

$$\phi^{level} = \hat{\phi}_{\beta_1+\beta_2}^{level}.$$

Some remarks on this algorithm: First, the coarse-grid integral operator is constructed by re-discretizing the directional derivative of the streaming-collision operator and volume weighting or harmonic averaging the cross-section coefficients. More sophisticated albeit more computationally intensive procedures can be used to coarsen the cross-section coefficients. Second, spatial Nystrom interpolation (2.2) is used rather than (2.1) because the former scheme has better discretization accuracy. Lastly, the multilevel form of the multiple-coarsening scheme is obtained by recursively applying the two-grid cycle between each pair of successive angle levels.

This algorithm employs the coarsening scheme pictured in Figure 1.1. Taking the semi-coarsening viewpoint, where each spatial  $V(\beta_1, \beta_2)$  cycle is viewed as a spatial plane solve for an angle branch, this algorithm semi-coarsens in angle. Such coarsening follows from the spectral analysis of [9], which shows that the near-nullspace of integral equation (1.7) is indirectly smooth in angle. But, since the analysis of [9] does not reveal the spatial characteristics of the near-nullspace components, one might consider semi-coarsening in space. Corresponding to this semi-coarsening is the vertical tree structure of Figure 2.1, left. The inner  $V(\beta_1, \beta_2)$  cycles now will correspond to angular

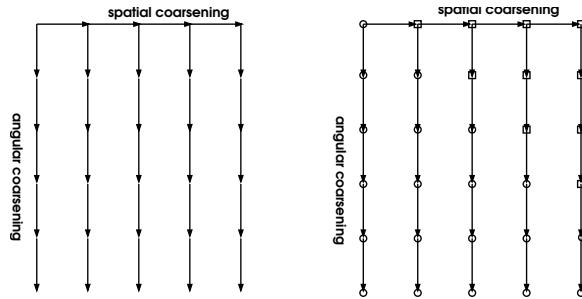


FIG. 2.1. *Spatial semi-coarsening. Right: relaxation performed only circled levels. This effectively resolves only smooth angular components on the coarser spatial levels.*

plane solves for the vertical branches of Figure 2.1. To realize this new semi-coarsening scheme, the inner/outer  $V$  cycles of the above pseudo-codes just have to be reversed.

Numerical results comparing the two multiple-coarsening/semi-coarsening schemes reveal that this spatial semi-coarsening method performs better than the original angle semi-coarsening of [8]. The experiments were performed for a Petrov-Galerkin spatial discretization of (1.1)-(1.2). The boundary conditions and total cross-sections are illustrated in Figure 2.2, where the checkerboard cross-section has jumps that are not grid-aligned on some of the coarser spatial levels. The scattering cross-section is

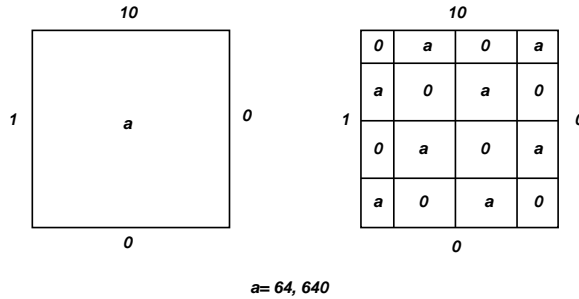


FIG. 2.2. *Problem setup: non-homogeneous inflow boundary conditions, constant and checkerboard total cross-sections. Note that the jumps in the discontinuous checkerboard cross-section are not grid-aligned on some of the coarser spatial levels.*

given by

$$\frac{\sigma_{s,0}}{\sigma_t} = 0.9999 \quad \frac{\sigma_{s,i}}{\sigma_t} = 0.9^i * (0.9999) \quad 0 < i \leq L,$$

so that some of the problems will involve optically thick and thin regions, with strong anisotropy. The target space-angle grid has a spatial meshsize of  $h = \frac{1}{128}$  and 64 angles. The spatial grid is coarsened by doubling the meshsize in each coordinate direction with the coarsest spatial grid consisting of 4 cells, and the angle grid is coarsened by halving the number of angles (i.e., choosing a quadrature rule with half the number of angles, thereby leading to non-nested angle grids) with the coarsest angle grid having  $[\max(2, L + 1)]^2$  angles to ensure accurate integration of all the scalar moments. The source term is 1 and the first scatter is the initial guess.  $V(\cdot, 0)$  cycles are used in the outer and inner iteration. The number of GMRES smoothing steps increases as the angle trunk/branches are descended:  $5 + 5 * (L_\Omega - l_\Omega)$  on level  $l_\Omega$ , and hence, the inner  $V(\cdot, 0)$  cycles have variable numbers of pre-smoothing steps, depending on the angle level. The stopping criterion is the residual norm to decrease by at least 8 orders of magnitude, although a 10-order reduction was observed in most of the runs. The number of outer  $V(1, 0)$  cycles are tabulated in Table 2.1, where “vertical tree” and “horizontal tree” indicate semi-coarsening in space and angle, respectively.

Problem	a	Method	L			
			0	1	2	3
constant coeffs.	64	vertical tree	3	3	4	4
		horizontal tree	5	6	5	5
	640	vertical tree	5	6	6	10
		horizontal tree	6	9	9	10
discontinuous coeffs.	64	vertical tree	4	5	5	5
		horizontal tree	5	6	6	5
	640	vertical tree	10	8	9	9
		horizontal tree	10	13	15	13

TABLE 2.1

*Petrov-Galerkin: constant/discontinuous coefficients, anisotropic (strong) scattering, 64 angles. “vertical tree”= semi-coarsening in space; “horizontal tree”= semi-coarsening in angle.*

There is alot that can be extracted or conjectured from this data.

**Spatial and angular semi-coarsening:** For isotropic scattering ( $L = 0$ ), both semi-coarsenings perform about the same, but for anisotropic scattering, semi-coarsening in space performs noticeably better. Viewing the inner  $V(\cdot, 0)$  cycles as plane solves, the isotropic scattering results indicate that the near-nullspace components are smooth in angle and space, and the anisotropic scattering results indicate that these components couple more strongly in angle, deduced from the improved performance using angle plane solves.

**Magnitude of  $\sigma_t$ :** To simplify our analysis, we isolate the effects due to coarse-grid operator inaccuracy by considering the constant coefficient results. Clearly, we see that increasing the magnitude of  $\sigma_t$  so that an optically thick problem arises, the convergence rate degrades. This convergence degradation is due to the introduction of some near-nullspace components ([9]). But since the performance for both semi-coarsening schemes degrade at about the same rate, it is unclear whether these near-nullspace components couple more strongly in space or angle.

**Coefficient discontinuities:** No surprise, the convergence rates for the discontinuous checkerboard cross-section are not as good as for the continuous cross-section. There are several possibilities for this. Since the discontinuities do not grid-align on some of the coarser spatial levels, one possible reason is poor coarse-grid approximation. But, when the discontinuities were adjusted to grid-align on all spatial levels, the convergence rates for both semi-coarsening methods did not substantially improve. Thus, another explanation has to be given. One possibility is that the near-nullspace components are more complex since the problem is optically thick in some regions and optically thin in other regions. A reasonable conjecture, based on a physical domain decomposition viewpoint, is that these components produce angular fluxes that are isotropic in the optically thick regions but anisotropic in the optically thin regions. The anisotropic property would imply that the problematic components are more strongly angle coupled than spatial coupled. However, these near-nullspace components do not have this mixed isotropic-anisotropic structure, as we will see in the next section.

**3. Spatial Description of the Near-Nullspace Components.** To derive a more thorough explanation of the results of the previous section, we need to carefully consider the near-nullspace components.

**3.1. Isotropic Scattering.** We initially assume isotropic scattering. Since there is no solver issues when the problem is optically thin everywhere, we assume that there are some subregions of  $R$  where the problem is optically thick. The continuous integral equation corresponding to (1.7) has the form

$$\phi(\mathbf{x}) - \int \mathbf{H}^{-1}[\sigma_s(\mathbf{x})\phi(\mathbf{x})] d\Omega = f(\mathbf{x}),$$

where  $\mathbf{H}$  is the streaming-collision operator ( $\Omega \cdot \nabla + \sigma_t$ ). A near-nullspace of this second-kind Fredholm equation satisfies

$$(3.1) \quad \phi(\mathbf{x}) \approx \int \mathbf{H}^{-1}[\sigma_s(\mathbf{x})\phi(\mathbf{x})] d\Omega := K\phi(\mathbf{x}),$$

where  $K$  is the integral operator. Equivalently,  $\phi$  is a near-nullspace of the integral equation if the solution  $w$  of

$$(3.2) \quad (\Omega \cdot \nabla + \sigma_t)w = \sigma_s\phi$$

is essentially isotropic and approximately equal to  $\phi$  itself. In this section, we construct some of these components using this equivalent description.

A near-nullspace component must have a small “energy” norm. Since  $(I - K)$  is generally non-self-adjoint, define the energy norm of  $\phi$  to be

$$(3.3) \quad \|\phi\|_{energy} = \sqrt{\frac{((I - K)\phi, (I - K)\phi)_{L^2(R)}}{(\phi, \phi)_{L^2(R)}}}.$$

If  $\phi$  is an eigenvector of  $(I - K)$  with corresponding eigenvalue  $\lambda$ , then its energy norm is  $|\lambda|$ , and if  $\phi$  is a near-nullspace of  $(I - K)$ , then its energy norm is  $\approx 0$ . We now construct a  $\phi$  with small energy norm.

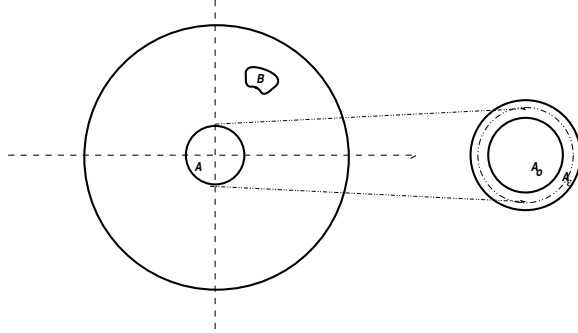


FIG. 3.1. Near-nullspace components can have several scales. In the circular domain  $R$ , the material is optically thick in subdomains  $A$  and  $B$ . Non-trivial near-nullspace components of several spatial scales exist for  $A$  and  $B$ . In the magnified image,  $\phi$  is 1 in the inner circle  $A_o$  and decays to zero in the outer annulus strip  $A_\epsilon$ .

Since we are considering near-nullspace components, we assume homogeneous boundary conditions for (3.2). Without loss of generality, we assume that the spatial domain  $R$  be a circle. Also, we assume that the cross-sections are piecewise constant functions, since this is most often the case in realistic applications. When the cross-sections are constant, the solution of (3.2) is

$$(3.4) \quad \begin{aligned} w(\mathbf{x}, \Omega) &= \int_0^{d_R(\mathbf{x}, \Omega)} e^{-\int_0^s \sigma_t(\mathbf{x} - t\Omega) dt} \sigma_s(\mathbf{x} - s\Omega) \phi(\mathbf{x} - s\Omega) ds \\ &= \int_0^{d_R(\mathbf{x}, \Omega)} \sigma_s e^{-\sigma_t s} \phi(\mathbf{x} - s\Omega) ds, \end{aligned}$$

where  $d_R(\mathbf{x}, \Omega)$  is the distant from  $\mathbf{x}$  to  $\partial R$  in the direction  $-\Omega$ , i.e.,  $d(\mathbf{x}, \Omega) = t > 0$ , with  $(\mathbf{x} - t\Omega) \in \partial R$ .

For an arbitrary  $\phi$ ,  $w$  is a function of  $\Omega$ , and hence, is not isotropic. We would like to determine  $\phi$ 's that produce  $w$ 's that are predominantly isotropic over most of  $R$ . Since  $w$  is isotropic if it is constant in  $\Omega$ , at any given spatial point  $\mathbf{x}$

$$(3.5) \quad \|w\|_{anisotropy} = \frac{\max_{\Omega_i, \Omega_j \in S^2} |w(\mathbf{x}, \Omega_i) - w(\mathbf{x}, \Omega_j)|}{|\int w(\mathbf{x}, \Omega) d\Omega|}$$

somewhat measures the degree of anisotropy. If this measure is small, then  $w$  is essentially isotropic at  $\mathbf{x}$ . We will use this measure or, if it is too difficult to evaluate, geometric reasoning to determine the degree of anisotropy.

Now, suppose the cross-sections are piecewise constant in  $R$  with subregions  $A$  and  $B$  where the problem is optically thick, see Figure 3.1. Consider subregion  $A$ . To construct a near-nullspace component, let  $A_o$  be the interior of  $A$  within a distance of  $\epsilon$  from the boundary of  $A$ , and let  $A_\epsilon$  denote the boundary strip of width  $2\epsilon$  that bounds  $A_o$  and extends a distance of  $2\epsilon$  from the boundary of  $A_o$  (see the magnified image of Figure 3.1). Width  $2\epsilon$  is determined by the magnitude of  $\sigma_t$ , with the width decreasing as the magnitude of  $\sigma_t$  increases. Define  $\phi$  to be the non-negative function

$$(3.6) \quad \phi(\mathbf{x}) = \begin{cases} 1 & \mathbf{x} \in A_o \\ 0 & \mathbf{x} \in R \setminus (A \cup A_\epsilon) \\ \rightarrow 0^+ & \mathbf{x} \in A_\epsilon, \end{cases}$$

where the expression “ $\rightarrow 0^+$ ” denotes  $\phi$  approaching  $0^+$  sufficiently fast as  $\mathbf{x}$  approaches the boundary of  $A$ , and sufficiently fast in the sense that for any angle  $\Omega \in S^2$ ,

$$(3.7) \quad \int_{d_1}^{d_2} e^{-\int_0^s \sigma_t(\mathbf{x}-t\Omega) dt} \sigma_s(\mathbf{x}-s\Omega) \phi(\mathbf{x}-s\Omega) ds \ll 1,$$

where  $d_1$  and  $d_2$  are respectively the distance between  $\mathbf{x}$  and the tail and head of the segment of the ray in  $A_\epsilon$  (see Figure 3.2). So, for  $\mathbf{x}$  in the interior of  $A_o$ ,

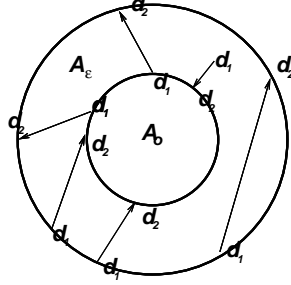


FIG. 3.2. Segments of ray-traced vector in  $A_\epsilon$ .  $d_1$  is the distance between the point  $\mathbf{x}$  (not shown) and the beginning of the segment, and  $d_2$  is the distance between this point and the end of the segment.

$$(3.8) \quad \begin{aligned} w(\mathbf{x}, \Omega) &= \int_0^{d_R(\mathbf{x}, \Omega)} e^{-\int_0^s \sigma_t(\mathbf{x}-t\Omega) dt} \sigma_s(\mathbf{x}-s\Omega) \phi(\mathbf{x}-s\Omega) ds \\ &= \int_0^{d_{A \cup A_\epsilon}(\mathbf{x}, \Omega)} e^{-\int_0^s \sigma_t(\mathbf{x}-t\Omega) dt} \sigma_s(\mathbf{x}-s\Omega) \phi(\mathbf{x}-s\Omega) ds \\ &\approx \sigma_s \int_0^{d_{A_o}(\mathbf{x}, \Omega)} e^{-\sigma_t s} ds \\ &= \frac{\sigma_s}{\sigma_t} (1 - e^{-\sigma_t d_{A_o}(\mathbf{x}, \Omega)}) \end{aligned}$$

(see Figure 3.3). The degree of anisotropy for  $w$  is

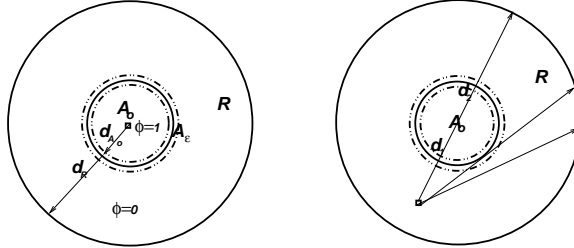


FIG. 3.3. Ray-traced solution at  $\mathbf{x}$ =centre point of  $A_o$  and at a point in  $R \setminus A$ .

$$\begin{aligned} \|w\|_{anisotropy} &\approx \frac{e^{-\sigma_t d_{\min}} - e^{-\sigma_t d_{\max}}}{\int (1 - e^{-\sigma_t d_{A_o}(\mathbf{x}, \Omega)}) d\Omega} \\ &\approx (e^{-\sigma_t d_{\min}} - e^{-\sigma_t d_{\max}}), \end{aligned}$$

since the cross-section is optically thick, i.e.,  $\sigma_t \gg 1$ . Here, we assumed  $\int d\Omega = 1$ , and denoted by  $d_{\min}$  and  $d_{\max}$  the distance  $d_{A_o}(\mathbf{x}, \Omega)$  where  $\max_{\Omega_i \in S^2} w(\mathbf{x}, \Omega_i)$  and  $\min_{\Omega_i \in S^2} w(\mathbf{x}, \Omega_i)$  occurs, respectively. Again, because the problem is optically thick in  $A$ ,  $\|w\|_{anisotropy} \approx 0$ , so that  $w$  is essentially isotropic for any point in the interior

of  $A_o$ . Moreover, in the interior of  $A_o$ ,  $w$  is approximately equal to  $\phi$  itself:

$$\begin{aligned} w(\mathbf{x}, \Omega) &\approx \frac{\sigma_s}{\sigma_t} (1 - e^{-\sigma_t d_{A_o}(\mathbf{x}, \Omega)}) \\ &\approx 1 \\ &= \phi(\mathbf{x}). \end{aligned}$$

Thus, inside  $A_o$ ,  $\phi$  behaves like a near-nullspace component of  $(I - K)$ .

Consider a point  $\mathbf{x}$  in  $R \setminus (A \cup A_\epsilon)$ . Three rays emanating from such a point are shown in Figure 3.3, with one ray crossing  $A_o$ , another tangent to it, and one completely missing it. These are the only possible cases. In the last case, for these  $\Omega$ 's, since  $\phi = 0$  outside of  $(A \cup A_\epsilon)$ ,  $w(\mathbf{x}, \Omega) = 0$ . In the second case, for these  $\Omega$ 's, using (3.7),  $w(\mathbf{x}, \Omega) \approx 0$ . In the first case, using (3.7),

$$\begin{aligned} w(\mathbf{x}, \Omega) &= \int_0^{d_R(\mathbf{x}, \Omega)} e^{-\int_0^s \sigma_t(\mathbf{x} - t\Omega) dt} \sigma_s(\mathbf{x} - s\Omega) \phi(\mathbf{x} - s\Omega) ds \\ &\approx \sigma_s \int_{d_1}^{d_2} e^{-\sigma_t s} ds \\ (3.9) \quad &= \frac{\sigma_s}{\sigma_t} (e^{-\sigma_t d_1} - e^{-\sigma_t d_2}), \end{aligned}$$

where  $d_1$  and  $d_2$  are the distance between  $\mathbf{x}$  and the tail and head of the ray segment in  $A_o$  (see Figure 3.3, right). Because the material is optically thick in  $A$ ,

$$(e^{-\sigma_t d_1} - e^{-\sigma_t d_2}) \approx 0.$$

Thus, for  $\mathbf{x} \in (A \cup A_\epsilon)$ ,  $w(\mathbf{x}, \Omega) \approx 0$ . Since this is true independent of  $\Omega$ , geometrically then,  $w$  is essentially isotropic.

Lastly, consider a point  $\mathbf{x} \in A_\epsilon$ . Two rays emanating from such a point is illustrated in Figure 3.4. For an angle  $\Omega$  leading to a ray that misses  $A_o$ , using (3.7),  $w(\mathbf{x}, \Omega) \approx 0$ . However, for an angle that leads to a ray that crosses through  $A_o$ ,

$$(3.10) \quad w(\mathbf{x}, \Omega) = \frac{\sigma_s}{\sigma_t} (e^{-\sigma_t d_1} - e^{-\sigma_t d_2}).$$

Depending on how close  $\mathbf{x}$  is to the boundary of  $A_o$ ,

$$w(\mathbf{x}, \Omega) \approx \frac{\sigma_s}{\sigma_t} e^{-\sigma_t d_1} < \frac{\sigma_s}{\sigma_t} \approx 1.$$

Hence, for any angle, using the positivity of  $\phi$  and  $w$

$$\begin{aligned} |(I - K)\phi| &= \left| \phi - \int w d\Omega \right| \\ (3.11) \quad &\approx \left| 0^+ - \int w d\Omega \right| < 1. \end{aligned}$$

Moreover, note that the degree of anisotropy can be large since  $w(x, \Omega)$  is approximately  $\frac{\sigma_s}{\sigma_t} e^{-\sigma_t d_1}$  for some directions (and dependent on these direction) and 0 for other directions.

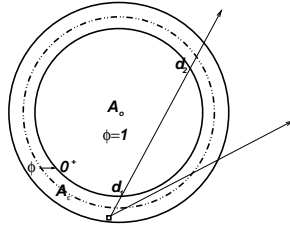


FIG. 3.4. Ray-traced solutions for a point in  $A_\epsilon$ .

Hence, for  $\phi$  given by (3.6), we have

$$(3.12) \quad [(I - K)\phi](\mathbf{x}) \begin{cases} \approx 0 & \mathbf{x} \in A_o \\ \approx 0 & \mathbf{x} \in R \setminus (A \cup A_\epsilon) \\ < 1 & \mathbf{x} \in A_\epsilon. \end{cases}$$

Let  $\delta$  be the area of  $A_\epsilon$  and  $|A_o|$  the area of  $A_o$ . Then

$$(3.13) \quad \begin{aligned} \|\phi\|_{energy} &= \sqrt{\frac{((I - K)\phi, (I - K)\phi)_{L^2(R)}}{(\phi, \phi)_{L^2(R)}}} \\ &\approx \sqrt{\frac{\int_{A_\epsilon} [(I - K)\phi]^2(\mathbf{x}) d\mathbf{x}}{\int_{A_o} \phi^2(\mathbf{x}) d\mathbf{x}}} \\ &< \sqrt{\frac{\delta}{|A_o|}}. \end{aligned}$$

Depending on the magnitude of  $\sigma_t$ , this norm is small, and so, (3.6) is a near-nullspace of the  $[I - K]$ .

This near-nullspace component can be described as a spatially smooth function in  $R$  minus the small boundary strip  $A_\epsilon$ . Such a component can be constructed for each subregion where the problem is optically thick. Depending on the size of these subregions, the near-nullspace components will have multiple spatial scales.

On the hand, consider a  $\phi$  that is highly spatially varying. In general,

$$w(\mathbf{x}, \Omega) = \int_0^{d_R(\mathbf{x}, \Omega)} e^{-\int_0^s \sigma_t(\mathbf{x} - t\Omega) dt} \sigma_s(\mathbf{x} - s\Omega) \phi(\mathbf{x} - s\Omega) ds$$

will be anisotropic in  $\Omega$ . Its projection onto the spherical harmonic  $Y_{00}$  will be generally small. Thus,  $[I - K]\phi$  will be non-zero and relatively large everywhere, implying that the energy norm of  $\phi$  will be relatively large. In fact, if we assume that the cross-sections are constant in  $R$ , then by converting from polar/spherical coordinates to Cartesian coordinates, we have

$$(3.14) \quad \begin{aligned} \int w(\mathbf{x}, \Omega) d\Omega &= \int \int_0^{d_R(\mathbf{x}, \Omega)} e^{-\int_0^s \sigma_t(\mathbf{x} - t\Omega) dt} \sigma_s(\mathbf{x} - s\Omega) \phi(\mathbf{x} - s\Omega) ds d\Omega \\ &= \int_R \frac{e^{-\sigma_t|\mathbf{x} - \mathbf{y}|}}{|\mathbf{x} - \mathbf{y}|} \sigma_s \phi(\mathbf{y}) d\mathbf{y}. \end{aligned}$$

This shows that  $K\phi$  is a global smoothing or weighted average of  $\phi$  itself. Since  $\phi$  is spatially varying,  $(\phi - K\phi)$  will be non-trivial. This, in turn, shows that the energy norm of  $\phi$  is generally relatively large.

We have shown that a smooth frequency of  $(I - K)$  must be spatially smooth, and if  $\phi$  is spatially oscillatory, then it has large energy norm. On the other hand, if  $\phi$  is a high frequency of  $(I - K)$ , then  $K\phi \approx 0$ . This means that the solution  $w$  of (3.2) is highly angle dependent, which means that  $\phi$  is spatially oscillatory (i.e., the integrand  $\sigma_s e^{-\sigma_t s} \phi(\mathbf{x} - s\Omega)$  must vary strongly in  $(\mathbf{x} - s\Omega)$  for  $w$  to be highly angle dependent. This, in turn, implies that  $\phi$  is strongly spatially varying).

We have verified that a near-nullspace has the form (3.6) when  $R$  and  $A$  are simple circles. For arbitrary shapes, as illustrated in Figure 3.5, the form of the near-nullspace components will have the same basic smooth structure of (3.6). Moreover, we have shown that the near-nullspace components do not generate angular fluxes that are essentially isotropic in the optically thick subregions and anisotropic in the optically thin subregions, as discussed at the end of Section 2. This, of course, can be deduced from (3.1), since if the angular flux is anisotropic, then  $K\phi \approx 0$  but  $\phi \neq 0$ .

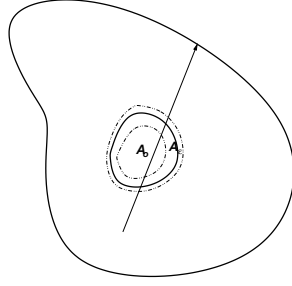


FIG. 3.5. Ray-traced solution in an arbitrary shaped domain  $R$  with an arbitrary shaped subregion  $A$ .

**3.2. Anisotropic Scattering.** The unknowns for the Boltzmann equation with anisotropic scattering are the scalar moments. The continuous integral equation has the form

$$\begin{pmatrix} \phi_{0,0}(\mathbf{x}) \\ \phi_{1,-1}(\mathbf{x}) \\ \vdots \\ \phi_{L,L}(\mathbf{x}) \end{pmatrix} - \begin{pmatrix} \int Y_{00}(\Omega) \mathbf{H}^{-1} [\sum_{lm} Y_{lm}(\Omega) \sigma_{s,l} \phi_{l,m}(\mathbf{x})] d\Omega \\ \int Y_{1,-1}(\Omega) \mathbf{H}^{-1} [\sum_{lm} Y_{lm}(\Omega) \sigma_{s,l} \phi_{l,m}(\mathbf{x})] d\Omega \\ \vdots \\ \int Y_{L,L}(\Omega) \mathbf{H}^{-1} [\sum_{lm} Y_{lm}(\Omega) \sigma_{s,l} \phi_{l,m}(\mathbf{x})] d\Omega \end{pmatrix} = \begin{pmatrix} f_{0,0}(\mathbf{x}) \\ f_{1,-1}(\mathbf{x}) \\ \vdots \\ f_{L,L}(\mathbf{x}) \end{pmatrix}$$

or, in operator notation,

$$(\mathcal{I} - \mathcal{K}) \phi = \mathbf{f}.$$

We see that the solution of the streaming-collision equation is now projected onto the first  $(L+1)^2$  spherical harmonics, rather than just the zero'th spherical harmonic as in the isotropic case. Obviously, the near-nullspace components of this integral equation are more complex than the ones in the isotropic case, one complexity being that they are vector functions. We will consider first a special set of these components, and then show that these are generally the only troublesome components.

This special set consists of zero-padded functions. Consider the zero-padded functions  $\phi_{lm} = (0, 0, \dots, \phi_{lm}, 0, \dots, 0)^t$ , which has a non-zero scalar function only in the  $lm$ 'th position. Assume again that in subregion  $A$ , the problem is optically thick in the sense that  $\frac{\sigma_{s,0}}{\sigma_t} \approx 1$  and  $\sigma_t \gg 1$ . Let  $R$  be decomposed into  $A_o$ ,  $A_\epsilon$  and  $R \setminus (A \cup A_\epsilon)$ , and let  $\phi_{lm}$  be given by (3.6) but with the condition that

$$(3.15) \quad \int_{d_1}^{d_2} e^{-\int_0^s \sigma_t(\mathbf{x}-t\Omega) dt} \sigma_{s,l}(\mathbf{x}-s\Omega) \phi_{lm}(\mathbf{x}-s\Omega) ds \ll 1$$

in  $A_\epsilon$ . The streaming-collision problem becomes

$$(3.16) \quad (\Omega \cdot \nabla + \sigma_t) w = \sigma_{s,l} \phi_{lm} Y_{lm}$$

and its solution is

$$\begin{aligned} w(\mathbf{x}, \Omega) &= \int_0^{d_R(\mathbf{x}, \Omega)} e^{-\int_0^s \sigma_t(\mathbf{x}-t\Omega) dt} \sigma_{s,l}(\mathbf{x}-s\Omega) \phi_{lm}(\mathbf{x}-s\Omega) Y_{lm}(\Omega) ds \\ &= Y_{lm}(\Omega) \int_0^{d_R(\mathbf{x}, \Omega)} e^{-\int_0^s \sigma_t(\mathbf{x}-t\Omega) dt} \sigma_{s,l}(\mathbf{x}-s\Omega) \phi_{lm}(\mathbf{x}-s\Omega) ds \\ (3.17) \quad &:= Y_{lm}(\Omega) \hat{w}(\mathbf{x}, \Omega). \end{aligned}$$

Similar to the derivation in the previous subsection, we have

$$(3.18) \quad \hat{w}(\mathbf{x}) \begin{cases} \approx \frac{\sigma_{s,l}}{\sigma_t} & \mathbf{x} \in A_o \\ \approx 0 & \mathbf{x} \in R \setminus (A \cup A_\epsilon) \\ < 1 & \mathbf{x} \in A_\epsilon, \end{cases}$$

and  $\hat{w}(\mathbf{x}, \Omega)$  is essentially isotropic in  $R \setminus A_\epsilon$ . Projecting  $Y_{lm}(\Omega)\hat{w}(\mathbf{x}, \Omega)$  onto the first  $(L+1)^2$  spherical harmonics produces

$$\mathcal{K}\phi_{lm} \approx \begin{pmatrix} 0 \\ \vdots \\ \frac{\sigma_{s,l}}{\sigma_t}\phi_{l,m}(\mathbf{x}) \\ 0 \\ \vdots \\ 0 \end{pmatrix} \quad \mathbf{x} \in A_o \quad \text{and} \quad \mathcal{K}\phi_{lm} \approx \mathbf{0} \quad \mathbf{x} \in R \setminus (A \cup A_\epsilon).$$

In  $A_\epsilon$ , determining  $\mathcal{K}\phi_{lm}$  is more difficult because, there,  $\hat{w}(\mathbf{x}, \Omega)$  is anisotropic in  $\Omega$ . Let

$$\hat{w}(\mathbf{x}, \Omega) = \sum_{rs} \hat{w}_{rs}(\mathbf{x})Y_{rs}(\Omega), \quad \mathbf{x} \in A_\epsilon, \quad |\hat{w}_{rs}(\mathbf{x})| < 1,$$

be the spherical harmonic expansion of  $\hat{w}(\mathbf{x}, \Omega)$ . Projecting

$$Y_{lm}(\Omega)\hat{w}(\mathbf{x}, \Omega) = \sum_{rs} \hat{w}_{rs}(\mathbf{x})Y_{lm}(\Omega)Y_{rs}(\Omega)$$

onto the first  $(L+1)^2$  spherical harmonics now involves the inner products of three spherical harmonics,

$$\int Y_{l'm'}(\Omega)Y_{lm}(\Omega)Y_{rs}(\Omega) d\Omega.$$

These are given by Wigner 3j-symbols ([23]) and are non-zero only if

$$m' + m = s \quad \text{and} \quad |l' - l| \leq r \leq (l' + l).$$

Nevertheless, we have constants  $c_{ij}$  such that

$$(\mathcal{I} - \mathcal{K})\phi_{lm} < \begin{pmatrix} c_{00} \\ c_{1,-1} \\ \vdots \\ c_{LL} \end{pmatrix} \quad \mathbf{x} \in A_\epsilon.$$

We further have

$$(\mathcal{I} - \mathcal{K})\phi_{lm} \approx \begin{pmatrix} 0 \\ \vdots \\ (1 - \frac{\sigma_{s,l}}{\sigma_t}) \\ 0 \\ \vdots \\ 0 \end{pmatrix} \quad \mathbf{x} \in A_o \quad \text{and} \quad (\mathcal{I} - \mathcal{K})\phi_{lm} \approx 0 \quad \mathbf{x} \in R \setminus (A \cup A_\epsilon).$$

Letting  $\delta$  and  $|A_o|$  denote the areas of  $A_\epsilon$  and  $A_o$  again, the energy norm of  $\phi_{lm}$  is

$$(3.19) \quad \|\phi_{lm}\|_{energy} < \sqrt{\frac{\left(1 - \frac{\sigma_{s,l}}{\sigma_t}\right)^2 |A_o| + C\delta}{|A_o|}}.$$

Since the problem is optically thick in  $A_o$ , we can assume that  $\delta$  is sufficiently small so that this norm is approximately  $\left(1 - \frac{\sigma_{s,l}}{\sigma_t}\right)$ . Hence, for  $l$ 's with  $\sigma_{s,l} \approx \sigma_t$ , the zero-padded  $\phi_{lm}$ 's with  $\phi_{lm}$  spatially defined by (3.6) are near-nullspace components of  $(\mathcal{I} - \mathcal{K})$ . For  $l$ 's with  $\sigma_{s,l} < \sigma_t$ , the corresponding  $\phi_{lm}$ 's will give large energy norms, and thus, are high frequencies.

Note that in  $A_\epsilon$ ,  $\phi_{lm}$  couples to the other  $((L+1)^2 - 1)$  moments. Fortunately, this coupling is only weak. However, if  $lm$ 'th element of  $\phi_{lm}$  spatially varies, the coupling will be strong. In this case,  $\hat{w}(\mathbf{x}, \Omega)$  is generally anisotropic over all of  $R$ . Expanding  $\hat{w}(\mathbf{x}, \Omega)$  in spherical harmonics, then

$$(\mathcal{I} - \mathcal{K})\phi_{lm} \approx \begin{pmatrix} -c_{00}\hat{w}_{00}(\mathbf{x}) \\ -c_{1,-1}\hat{w}_{1,-1}(\mathbf{x}) \\ \vdots \\ \phi_{lm}(\mathbf{x}) - c_{lm}\hat{w}_{lm}(\mathbf{x}) \\ -c_{l,m+1}\hat{w}_{l,m+1}(\mathbf{x}) \\ \vdots \\ c_{LL}\hat{w}_{LL}(\mathbf{x}) \end{pmatrix} \quad \mathbf{x} \in R,$$

which shows that  $(\mathcal{I} - \mathcal{K})$  strongly couples all the moments. We also see that the energy norm for this  $\phi_{lm}$  is generally large.

Summarizing, some of the near-nullspace components of  $(\mathcal{I} - \mathcal{K})$  are the zero-padded  $\phi_{lm}$  with  $\phi_{lm}$  of the form (3.6) and  $\sigma_{s,l} \approx \sigma_t$  in  $A$ . Similar near-nullspace components for other subregions where the cross-sections are optically thick can be constructed. Furthermore, zero-padded  $\phi_{lm}$ 's with  $\sigma_{s,l} < \sigma_t$  or  $\phi_{lm}$  spatially rough are high frequencies of  $(\mathcal{I} - \mathcal{K})$ .

Now, denote the set of zero-padded near-nullspace components by  $\mathcal{N}$  and let  $\mathcal{SN}$  be the linear span of  $\mathcal{N}$ ,

$$(3.20) \quad \mathcal{SN} = \left\{ \phi \mid \phi = \sum_i a_i \phi_i, \phi_i \in \mathcal{N} \right\}.$$

Consider a vector  $\boldsymbol{\eta} = (\phi_{00}, \phi_{1,-1}, \dots, \phi_{LL})^t$ . The angular flux  $w$  satisfies

$$(3.21) \quad (\Omega \cdot \nabla + \sigma_t)w = \sum_{lm} \sigma_{s,l} \phi_{lm} Y_{lm}, \quad l = 0, \dots, L, \quad -l \leq m \leq l.$$

It can be solved by superpositioning the solutions of

$$(3.22) \quad (\Omega \cdot \nabla + \sigma_t)w_{lm} = \sigma_{s,l} \phi_{lm} Y_{lm},$$

i.e.,  $w = \sum_{lm} w_{lm}$ . Clearly, if  $\boldsymbol{\eta} \in \mathcal{SN}$ , then it is a near-nullspace of  $(\mathcal{I} - \mathcal{K})$ . If  $\boldsymbol{\eta} \notin \mathcal{SN}$ , then there must be at least one  $\phi_{lm}$  that is spatially oscillatory or with  $\sigma_{s,l} < \sigma_t$ . By superposition,  $w(\mathbf{x}, \Omega)$  is anisotropic in  $\Omega$ , and the energy norm of  $\boldsymbol{\eta}$  will be large. Hence, the near-nullspace of  $(\mathcal{I} - \mathcal{K})$  is  $\mathcal{SN}$ .

#### 4. Improved Multiple-Coarsening Scheme.

**4.1. Appropriate Space-Angle Grids.** So, for either isotropic or anisotropic scattering, the near-nullspace components are constructed from smooth functions of the form (3.6) in subregions where the cross-sections are optically thick ( $\frac{\sigma_s}{\sigma_t} \approx 1$  or  $\frac{\sigma_{s,l}}{\sigma_t} \approx 1$ , and  $\sigma_t \gg 1$ ). This is a spatial description of these troublesome components. Also, a spatial characteristic of the high frequencies of the integral equation is spatial roughness. In fact, even relatively mild spatial variation can lead to moderate frequencies.

In contrast, in [9], an ‘‘angular description’’ of the near-nullspace components was given: for isotropic scattering,  $\phi$  is a near-nullspace component if the angular flux  $\psi$  generated by  $\phi$  (i.e.,  $(\Omega \cdot \nabla + \sigma_t)\psi = \sigma_s \phi$ ) is smooth in angle or equivalently, its spherical harmonic expansion is dominated by the zero'th-order term. Hence, near-nullspace error components can be eliminated efficiently on coarse angle grids. Also, in [9], high frequencies were described as scalar fluxes that generate angular fluxes with spherical harmonic expansions having large contributions from the higher-order terms. This implies that the angular fluxes corresponding to these scalar fluxes are

strongly coupled or dependent on  $\Omega$ , i.e., strongly non-smooth in  $\Omega$ . In the isotropic case, these angular fluxes have the form

$$\psi(\mathbf{x}, \Omega) = \sum_{lm} \psi_{lm}(\mathbf{x}) Y_{lm}(\Omega).$$

In the anisotropic case, they have the form

$$\begin{aligned} \psi(\mathbf{x}, \Omega) &= \sum_{lm} \hat{\psi}_{lm}(\mathbf{x}, \Omega) Y_{lm}(\Omega) \\ (4.1) \qquad &= \sum_{lm} \sum_{rs} \hat{\psi}_{lm,rs}(\mathbf{x}) Y_{lm}(\Omega) Y_{rs}(\Omega), \end{aligned}$$

where  $\hat{\psi}_{lm}(\mathbf{x}, \Omega)$  is the angle anisotropic function

$$\hat{\psi}_{lm}(\mathbf{x}, \Omega) = \int_0^{d_R(\mathbf{x}, \Omega)} e^{-\int_0^s \sigma_t(\mathbf{x}-t\Omega) dt} \sigma_{s,l}(\mathbf{x}-s\Omega) \phi_{lm}(\mathbf{x}-s\Omega) ds.$$

This shows that angle oscillations are stronger in the anisotropic case (product  $Y_{lm}(\Omega)Y_{rs}(\Omega)$  compared to  $Y_{lm}(\Omega)$ ), and taking into consideration that moderate frequencies can be mildly spatially varying, angle plane solve is more appropriate than spatial plane solve for attenuating these frequencies. This explains the better convergence rates for the spatial semi-coarsening method for the examples in Section 2.

Now, although the descriptions of the frequencies were derived in continuum, a complete discretization of the Boltzmann equation leads to an approximation of the integral equation. Good discretization accuracy to the integral equation can be attained by using an accurate quadrature rule with symmetric quadrature points, i.e., both angles  $\Omega_i$  and  $-\Omega_i$  are used. Such a choice leads to cancellation of the discretization errors in the streaming operators. Assuming good accuracy then, another deduction can be extracted from the spatial and angle descriptions of the frequencies. This is the appropriate space-angle grids to use in a multiple-coarsening method. Since the near-nullspace is smooth in space and angle (indirectly) and the high frequencies are rough in space and angle, coarse space grids should be introduced incrementally as the angle grid is coarsened (see Figure 4.1). Because the near-nullspace components spatially vary in the boundary strips of the optically thick subregions, fine space grids should also be used on the coarser angle levels. These are the space-angle grids that are needed in the multiple-coarsening algorithm. Of course, the whole spatial grid hierarchy can be used on all angle levels, as in the original method of [8]. But the convergence improvement obtained by using these additional spatial grids may not warrant the additional computational cost required for using the additional spatial grids.

Applying the angular semi-coarsening method on these space-angle grids produces the tree structure illustrated in Figure 1.2, left. If coarse space grids are introduced only on the coarsest angle level, the tree structure illustrated in the right image of Figure 1.2 is produced. And, if the spatial semi-coarsening scheme is restricted to these appropriate space-angle grids, the tree structure of the right image of Figure 2.1 is produced. This restricted scheme can be realized by omitting relaxing on some of the coarse space grids on the finer angle levels.

To demonstrate the performance of these new schemes, we apply them to the examples of Section 2, using a variety of space-angle grids to assess the veracity of the above analysis. The grids are illustrated in Figure 4.2. Tree 1 progressively introduces the spatial coarse grid hierarchies in a fashion described in Figure 4.1. This will ensure that the smoother frequencies are progressively captured on the coarser angle levels. In contrast, Tree 2 introduces a spatial coarse grid hierarchy only on the coarsest angle level. Although the spatially smooth near-nullspace components

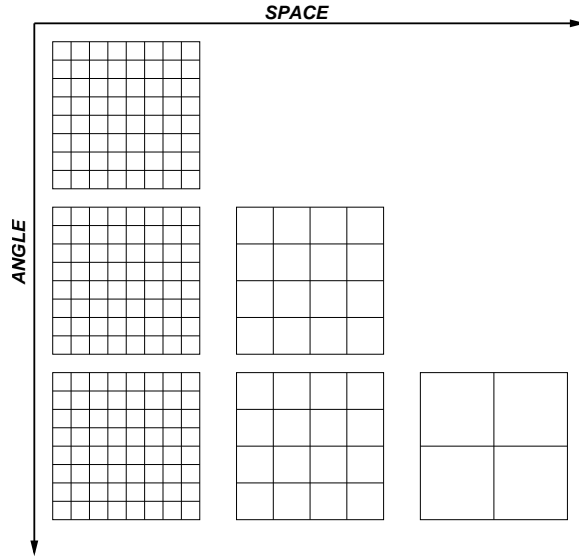


FIG. 4.1. The spatial grid hierarchy should be introduced only on the coarser angle levels since the near-nullspace components are smooth in angle and space. Finer spatial grids are needed on the coarser angle levels because of the spatial oscillations in the near-nullspace components in  $A_\epsilon$ .

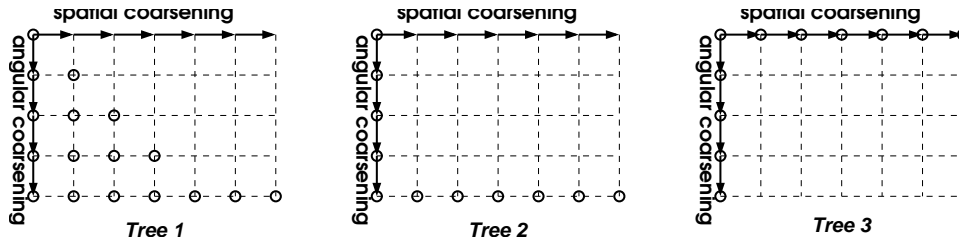


FIG. 4.2. Space-angle grids used in the multiple-coarsening/semi-coarsening algorithms. Circled space-angle levels indicate that that space-angle grid is actively used. Trees 1 and 2 introduce spatial coarse grid hierarchies on the coarse angle levels, where the spatially smooth near-nullspace components are representable. Tree 3 introduces a spatial coarse grid hierarchy only on the finest angle level, and hence, the multigrid algorithm using these space-angle grids will not effectively eliminate the near-nullspace components.

will be representable on the coarsest angle level, intermediate frequencies might not be adequately represented on only the finest spatial grid of the finer angle levels. This can affect the multigrid convergence rate. Lastly, Tree 3 introduces a spatial coarse grid hierarchy only on the finest angle level. The space-angle grids of this tree will not be sufficient to represent both the near-nullspace components and other smoother frequencies. Thus, we expect the multigrid method using Tree 1 will perform better than using Tree 2, which in turn, will be better than using Tree 3. Furthermore, particularly for anisotropic scattering, because the higher frequencies lead to strong angle oscillations and moment coupling, we expect the spatial semi-coarsening scheme to perform better than the angle semi-coarsening scheme. In fact, we expect the spatial semi-coarsening scheme with Tree 1 will perform just as well as the spatial semi-coarsening using the full spatial coarse grid hierarchies on all the angle levels. The results are given in Table 4.1.

Although overall the results agree with our expectations, some of the results expose the subtlety of the intrinsic space-angle coupling in the frequencies. Here are some observations:

**Spatial semi-coarsening:** As predicted, the convergence rate of this semi-coarsening method using the space-angle grids of Tree 1 is about the same as the rate when using

Semi-coarsening	Problem	a	Method	L			
				0	1	2	3
Spatial	constant coefs.	64	Tree 1	3	3	4	4
			Tree 2	3	4	4	4
			Tree 3	4	4	4	5
		640	Tree 1	6	7	6	12
			Tree 2	6	8	7	12
			Tree 3	11	20	19	31
	discontinuous coefs.	64	Tree 1	4	5	5	5
			Tree 2	4	5	5	5
			Tree 3	4	5	5	5
		640	Tree 1	12	10	9	11
			Tree 2	div.	13	9	12
			Tree 3	17	19	15	31
Angular	constant coefs.	64	Tree 1	6	10	10	9
			Tree 2	6	10	10	9
			Tree 3	5	6	5	6
		640	Tree 1	6	10	10	12
			Tree 2	7	10	10	12
			Tree 3	12	22	23	44
	discontinuous coefs.	64	Tree 1	7	11	11	10
			Tree 2	7	11	11	10
			Tree 3	5	6	6	5
		640	Tree 1	14	17	21	17
			Tree 2	18	30	22	18
			Tree 3	19	26	22	48

TABLE 4.1

*Petrov-Galerkin: constant/discontinuous coefficients, anisotropic (strong) scattering, 64 angles, spatial and angular semi-coarsening methods using the space-angle grids displayed in Figure 4.2.*

the full spatial grid hierarchy on all angle levels. At most, only two additional outer  $V(1,0)$  cycles are needed for this computationally cheaper method. This is true for isotropic and anisotropic scattering, optically thick ( $\sigma = 640$ ) and optically “thin” ( $\sigma = 64$ ) cross-sections, and for continuous and discontinuous cross-sections.

Also as predicted, using the space-angle grids of Tree 2, the convergence rate degrades when compared to the rate when using Tree 1. But this degradation is not as dramatic as expected, with degradation observed only in the optically thick problems. For the optically thin problems, the near-nullspace and intermediate smooth frequencies have only a minor impact on the convergence rate of the smoother itself, and thus, degradation is not observed when using Tree 2. For the optically thick problems, the degradation is rather minor, except when the scattering is isotropic and the cross-sections are discontinuous. In this case, the spatial semi-coarsening method diverges. Contrasting this to the convergence of the spatial semi-coarsening method using Tree 3, it appears that the problematic frequencies are spatially smooth but require more angles than the 4 that are used on the coarsest angle level of Tree 2. This angular anisotropy may be occurring along the boundary strips of the 8 optically thick subregions of the checkerboard pattern (see Figure 2.2, right). However, although this may be a partial explanation for the divergence, contrasting this divergence to the convergence of the angular semi-coarsening method using the same Tree 2 grids, the issue is more subtle. The difficulty may also be due to the intrinsic space-angle coupling of some of the frequencies. Indeed, recall that for isotropic scattering, the angle oscillations of the angular fluxes generated by the higher frequencies might be

only as rough as the spatial oscillations. This would indicate more subtle space-angle coupling for some of the frequencies, with attenuation of these frequencies better when using spatial plane solves, i.e., angular semi-coarsening.

Turning to Tree 3, as predicted, its convergence rate is not as good as Tree 2, with the exception of the divergence case. Slower convergence occurs for the optically thick problems, particularly for higher degrees of anisotropy. For these anisotropic problems, the number of zero-padded near-nullspaces increases as the degree increases. Since these angularly smooth components are not efficiently eliminated on the finest angle level, more outer  $V$ -cycles are needed.

**Angular semi-coarsening:** As can be observed from Table 4.1, angular semi-coarsening does not perform as well as spatial semi-coarsening, particularly for the anisotropic problems. As mentioned earlier, this is due to the strong angular oscillations of the angular fluxes generated by the higher frequencies of the integral equations. Because these angle oscillations are not treated well by this semi-coarsening method, the impact of the different space-angle grids is harder to determine for this method (i.e., the impact of the different grids is not isolated from the impact of angle oscillations). Nevertheless, for the optically thick problems, using Tree 1 performs better than using Tree 2, which in turn performs better than using Tree 3. But for the optically thin problems, using Tree 3 performs better than the other trees. It appears that the slowest converging modes are anisotropic in angle and thus more angles are required. But this is probably an artifact of poorly handling the strong angle oscillations in the angular fluxes generated by the higher frequencies, since the performance of the spatial semi-coarsening method is about the same for any of the trees for the optically thin problems.

**5. Conclusion.** In this paper, we have given both a spatial description and a refined angle-dependence description of the frequencies of the continuous integral equation corresponding to (1.7). These descriptions can be used to develop improved multiple-coarsening/semi-coarsening algorithms: the spatial description justifies using a reduced number of space-angle grids in the multiple-coarsening algorithm; the angle-dependence description permits the development of a spatial semi-coarsening scheme, which is more appropriate for anisotropic scattering problems. More importantly, these descriptions expose the intrinsic space-angle dependence of the frequencies of (1.7), which might prove useful for further analysis and development of multigrid methods for  $S_n$  discretizations of the Boltzmann transport equation.

#### REFERENCES

- [1] M. L. ADAMS AND E. W. LARSEN, *Fast iterative methods for discrete-ordinates particle transport calculations*, Progress in Nuclear Energy, 40, No. 1, 3-159 (2002).
- [2] R. E. ALCOUFFE, *Diffusion synthetic acceleration methods for the diamond-differenced discrete-ordinates equations*, Nucl. Sci. Eng., 64 (1977), pp. 344-355.
- [3] K. E. ATKINSON, *The Numerical Solution of Integral Equations of the Second Kind*, Cambridge University Press, 1997.
- [4] K. E. ATKINSON, *Iterative variants of the Nystrom method for the numerical solution of integral equations*, Numer. Math., 22 (1973), pp. 17-31.
- [5] P. N. BROWN, *A linear algebraic development of diffusion synthetic acceleration for three-dimensional transport equations*, SIAM J. Numer. Anal., 32 (1995), pp. 179-214.
- [6] S. L. CAMPBELL, I. C. F. IPSEN, C. T. KELLEY, AND C. D. MEYER, *GMRES and the minimal polynomial*, BIT, 36 (1996), pp. 664-675.
- [7] B. CHANG AND B. LEE, *A multigrid algorithm for solving the multi-group, anisotropic scattering Boltzmann equation using first-order system least-squares methodology*, ETNA, 15 (2003), pp. 132-151.
- [8] B. LEE, *A Novel Multigrid Method for  $S_n$  Discretizations of the Mono-Energetic Boltzmann Transport Equation in the Optically Thick and Thin Regimes with Anisotropic Scattering, Part I*, submitted to SISC.
- [9] B. LEE, *A Novel Multigrid Method for  $S_n$  Discretizations of the Mono-Energetic Boltzmann*

- Transport Equation in the Optically Thick and Thin Regimes with Anisotropic Scattering, Part II*, submitted to SISC.
- [10] B. LEE, *Energy-Space-Angle Multigrid Methods for Sn Discretizations of the Multiple Frequency Boltzmann Transport Equation*, submitted to SISC.
  - [11] R. DAUTRAY AND J. L. LIONS, *Mathematical Analysis and Numerical Methods for Science and Technology, Vol. 6*, Springer-Verlag, Berlin, 1993.
  - [12] C. C. DOUGLAS AND J. DOUGLAS, JR., *A unified convergence theory for abstract multigrid or multilevel algorithms, serial and parallel*, SIAM J. Numer. Anal., 30 (1993), pp. 136-158.
  - [13] W. HACKBUSCH, *Multi-Grid Methods and Applications*, Springer-Verlag, New York, 1985.
  - [14] L. HENYEY AND J. GREENSTEIN, *Diffuse radiation in the galaxy*, Astrophys. J., 93(1941), pp. 70-83.
  - [15] C. T. KELLEY, *Multilevel source iteration accelerators for the linear transport equation in slab geometry*, Transp. Th. Stat. Phys., 24 (1995), pp. 679-707.
  - [16] B. LEE, P. N. BROWN, AND T. A. MANTEUFFEL, *A moment-parity multigrid preconditioner for the first-order system least-squares formulation of the Boltzmann transport equation*, SIAM J. of Sci. Comp., 25 (2003), pp. 513-533.
  - [17] B. LEE, T. MANTEUFFEL, S. MCCORMICK, AND J. RUGE, *First-order system least-squares (fosl) for the Helmholtz equation* SIAM J. Sci. Comput., 21 (2000), pp. 1927-1949.
  - [18] P. LESAINTE AND P. A. RAVIART, *On a finite element method solving the neutron transport equation*, in Mathematical Aspects of Finite Elements in Partial Differential Equations, C. de Boor, ed., Academic Press, 1974.
  - [19] E. E. LEWIS AND W. F. MILLER, *Computational Methods of Neutron Transport*, John Wiley, 1984.
  - [20] R. L. LIBOFF, *Introductory Quantum Mechanics*, Holden-Day, Inc., San Francisco, 1980.
  - [21] M. SEAID AND A. KLAR, *Efficient preconditioning of linear systems arising from the discretization of radiative transfer equation*, in Lecture Notes in Computational Science and Engineering, 35 (2003), pp. 211-236.
  - [22] U. TROTTEBERG, C. W. OOSTERLEE, AND A. SCHULLER, *Multigrid*, Academic Press, 2001.
  - [23] Wigner 3j-symbol, <http://mathworld.wolfram.com/Wigner3j-Symbol.html>.